NANO LETTERS

Letter

pubs.acs.org/NanoLett

Syringe-Injectable Electronics with a Plug-and-Play Input/Output Interface

Thomas G. Schuhmann, Jr.,[†] Jun Yao,[‡] Guosong Hong,[‡] Tian-Ming Fu,[‡] and Charles M. Lieber*[,†,‡]

[†]John A. Paulson School of Engineering and Applied Sciences and [‡]Department of Chemistry and Chemical Biology, Harvard University, Cambridge, Massachusetts 02138, United States

Supporting Information

ABSTRACT: Syringe-injectable mesh electronics represent a new paradigm for brain science and neural prosthetics by virtue of the stable seamless integration of the electronics with neural tissues, a consequence of the macroporous mesh electronics structure with all size features similar to or less than individual neurons and tissue-like flexibility. These same properties, however, make input/output (I/O) connection to measurement electronics challenging, and work to-date has required methods that could be difficult to implement by the life sciences community. Here we present a new syringe-injectable mesh electronics design with plug-and-play I/O interfacing that is rapid, scalable, and user-friendly to nonexperts. The basic design tapers the ultraflexible mesh electronics to a narrow stem that routes all of the device/electrode interconnects to I/O pads that are inserted into a standard zero insertion force (ZIF) connector. Studies show that the entire plug-and-play mesh electronics can be delivered through capillary needles with precise targeting using microliter-scale injection volumes similar to the standard mesh electronics design. Electrical characterization of mesh electronics containing platinum (Pt) electrodes and silicon (Si) nanowire field-effect transistors (NW-FETs) demonstrates the ability to interface arbitrary devices with a contact resistance of only 3 Ω. Finally, in vivo injection into mice required only minutes for I/O connection and yielded expected local field potential (LFP) recordings from a compact head-stage compatible with chronic studies. Our results substantially lower barriers for use by new investigators and open the door for increasingly sophisticated and multifunctional mesh electronics designs for both basic and translational studies.

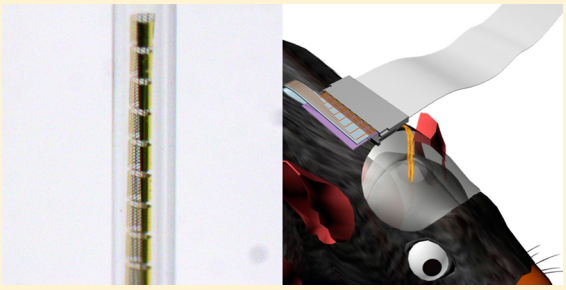

KEYWORDS: *Mesh electronics, neural interface, zero insertion force (ZIF) connection, flat flexible cable (FFC) connector, nanoelectronics interface, nanowire field-effect transistor*

Stable in vivo mapping of the same neurons and neural circuits over time could advance fundamental studies focused on understanding the brain as well as the application of neurotechnologies in medicine.[1,2] For example, the ability to record from individual neurons is a prerequisite to understanding the connectivity of neural circuits and how they give rise to the emergent functional properties of neuronal assemblies and networks.[3−5] Single neuron electrophysiology is also clinically important for applications ranging from improved decoding algorithm performance for brain−machine interfaces (BMIs) to understanding and potentially predicting epileptic seizures.[6−9] Electrical implants such as silicon probes and microwire tetrodes can enable single-neuron level mapping from shallow to deep brain regions, although these implants have generally been limited by mechanical mismatch and chronic immune responses that lead to an instability and degradation of recorded single neuron signals over days to weeks.[10−13] Recently, we have introduced a new paradigm for electrical implants based upon a macroporous, ultraflexible mesh structure that overcomes the long-standing limitations of conventional probes.[14−19] The underlying and unique design features of the mesh electronics include a macroporous overall structure with brain-like flexibility and feature sizes smaller than neurons.[14,20] These features allow the mesh electronics to be precisely implanted in targeted brain regions by syringe injection[15] and subsequently yield (i) seamless three-dimensional (3D) integration with neural tissue in vivo, (ii) an absence of the chronic immune response on at least months to a year timescale, which eliminates the typical glial scarring around implants,[21,22] and (iii) stable tracking of the same individual neurons and neural circuits on a timescale of at least one year without probe repositioning.[17]

The structural and mechanical properties of the mesh electronics that have led to these attractive properties as implants have also required specialized methods for making reliable I/O connections for measurement instrumentation. For example, initial studies used anisotropic conductive film (ACF) to electrically connect the mesh to an interface cable,[14] although the difficulty of aligning the ultraflexible mesh I/O pads to the cable as well as the elevated temperature and

Received: July 19, 2017
Revised: August 3, 2017
Published: August 8, 2017

DOI: 10.1021/acs.nanolett.7b03081
Nano Lett. 2017, 17, 5836−5842

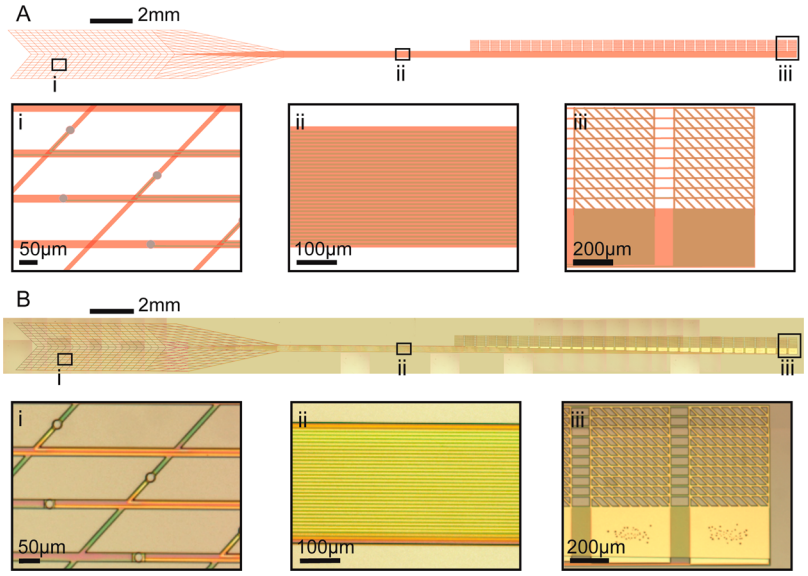

Figure 1. Overview of plug-and-play mesh electronics. (A) Schematic of syringe-injectable mesh electronics with plug-and-play I/O, with the ultraflexible mesh device region at left tapering into the flexible stem in the middle and I/O region at right. Insets provide magnified views of (i) Pt recording electrodes (gray circles) supported on the mesh, (ii) the thin film-like SU-8 stem containing independent metal interconnects for each electrode, and (iii) the I/O pads, each of which consists of an initial short continuous metal region followed by an ultraflexible mesh structured region; SU-8 only elements (horizontal lines) connect the mesh portions of the pads. (B) Tiled bright-field optical microscopy images of a representative syringe-injectable mesh electronics probe with plug-and-play I/O. The images were recorded prior to release of the probe from the fabrication substrate (Materials and Methods in Supporting Information); each image is about 1.4 × 1.7 mm^2. Insets (i), (ii), and (iii) are the same as the schematic regions shown in panel A.

pressure required for bonding made this difficult to implement reliably in a sterile surgical environment. Others have found success by employing temporary stiffeners or shuttle devices to implant flexible electronic probes in the brain after they have been bonded to an I/O interface.[16,23] These approaches simplify electrical I/O interfacing but lack the precise targeting of deep brain regions possible with stereotaxic injection of mesh electronics. Recently, we reported a computer-controlled conductive ink printing approach to define conductive lines between mesh I/O pads and conductors on a flat flexible cable (FFC) with excellent reliability.[15] An advantage of this strategy is that it can produce conductive lines over an irregular path to bond I/O pads when they are not spread linearly to match the FFC conductor spacing. Despite the success of this approach,[15,17] it does have limitations including (i) a connection time that scales linearly with the number of electrodes or devices, (ii) potential sterilization concerns for implementation in a human surgical environment, and (iii) the methodology is uncommon to neuroscience laboratories, which has led to a barrier for such researchers to implement mesh electronics.

To overcome these issues and make I/O interfacing to mesh electronics user-friendly for investigators independent of background, we have focused on a plug-and-play mesh electronics design (Figure 1A; Figure S1A–C) that incorporates several key features. First, it retains an ultraflexible mesh region, which is designed to extend from within the brain to outside the skull of the target animal, with either single terminal Pt metal (Figure 1A, i) or two terminal Si NW-FET (Figure S1B,C) recording devices. The design of this macroporous mesh region is similar to our previous reports that have demonstrated in vivo a minimal chronic immune response and stable long-term tracking of individual neurons.[14,17,18] Second, the mesh tapers outside of the skull to a stem region (Figure 1A, ii) that routes all of the interconnect lines from recording devices to I/O pads in a narrow continuous structure that can fit through the capillary needle inner diameter (I.D.) without deformation. Third, the stem transitions to an I/O region (Figure 1A, iii), where the array of I/O pads, which will plug into the interface connector, are oriented perpendicular to the parallel interconnect lines/longitudinal axis of the probe. The size and pitch of the array of I/O pads are designed to match a standard ZIF interface connector. The length of these pads must exceed the capillary needle I.D. to meet the goal of a facile "by hand" plug-and-play connection, and thus, we designed the I/O pads with a conducting mesh structure such that they roll-up within the capillary needle during loading but then unroll to their full size once ejected from the needle. The rhomboid lattice structure of the mesh minimizes bending stiffness in the transverse direction (normal to the mesh and capillary tube axes) while maximizing bending stiffness in the longitudinal direction (parallel to the mesh and capillary tube axes).[14]

We fabricated plug-and-play mesh electronics according to the above design in a wafer-based process similar to that used for previous free-standing and injectable mesh electronics (Materials and Methods in Supporting Information).[14−18,24,25] Briefly, we used photolithography to define a bottom layer of SU-8 polymer on a sacrificial relief layer. We then defined gold (Au) interconnects and Pt recording electrodes in two separate photolithography, evaporation, and lift-off processes, before passivating the interconnects with a top layer of SU-8 polymer that left the I/O pads and recording devices exposed on one side, and the Au interconnect lines encapsulated by the SU-8. Mesh electronics were fully released from their substrates by dissolving the sacrificial relief layer before rinsing and loading into capillary tubes for injection. For plug-and-play mesh electronics containing NW-FETs, Si NWs were aligned by contact printing onto a functionalized silica substrate.[26] The

DOI: 10.1021/acs.nanolett.7b03081
Nano Lett. 2017, 17, 5836−5842

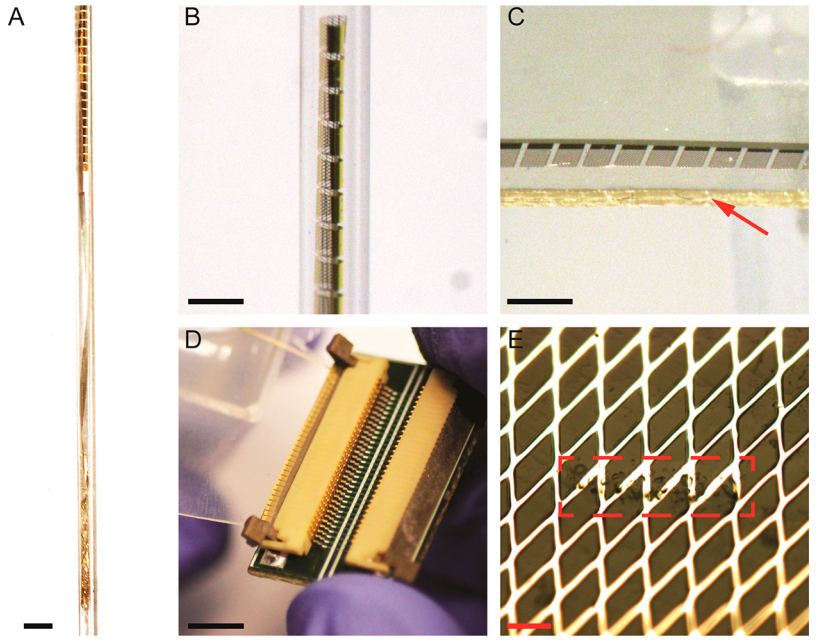

Figure 2. Loading, injection, and I/O interfacing of mesh electronics. (A) Photograph of mesh electronics loaded inside a 400 μm I.D. capillary tube. The I/O pads are visible near the top of the image, while the mesh device region is at bottom. Scale bar is 1 mm. (B) Photograph showing a magnified view of the I/O pads while rolled-up inside the capillary tube. Scale bar is 500 μm. (C) Photograph of the I/O pads after injecting the mesh device region into hydrogel and ejecting the I/O region onto a thin-film clamping substrate. The thin-film substrate has been trimmed to the I/O pad edges with scissors. The trimmed edge of the substrate is indicated by a red arrow. Scale bar is 1 mm. (D) Photograph of the I/O pads being inserted into the PCB-mounted ZIF connector. Scale bar is 5 mm. (E) Optical microscope image showing the indentation left on a mesh I/O pad after clamping/unclamping by a PCB-mounted ZIF connector. A red dashed box highlights the region of mechanical contact/deformation by one of the ZIF connector pins. Scale bar is 50 μm.

aligned NWs were then coated with poly(methyl methacrylate) (PMMA) and transferred to the bottom SU-8 layer before defining Au interconnects,[27,28] which in this case also served as metal−semiconductor contacts. The remaining fabrication steps for meshes containing NW-FETs were the same as for meshes containing only Pt electrodes.

The resulting plug-and-play mesh electronics were characterized by microscopy prior to release from their sacrificial relief layer. A single plug-and-play mesh occupying a rectangular area of about 2.2 × 38 mm^2 was imaged with micron resolution by tiling together individual bright-field optical microscope images each capturing an about 1.4 × 1.7 mm^2 field of view (FoV; Figure 1B). The tiled image highlights the key features of the plug-and-play mesh electronics design as fabricated, beginning with the device region at left, which contains Pt recording electrodes (Figure 1B, i) within an ultraflexible mesh structure that in two-dimensions (2D) is approximately 90% free space. The Au interconnects are visible at a density of two per longitudinal SU-8 element before terminating 1:1 on each circular Pt electrode. For Si NW-FET integrated meshes, dark-field optical imaging of a typical NW-FET in the device region (Figure S1D) shows Si NWs spanning the channel between a source and drain electrode.

Near the center of the tiled image, the ultraflexible mesh region tapers to the flexible, narrow stem (Figure 1B, ii), on which the electrode and/or NW-FET interconnects converge as they are carried toward the I/O region. In the I/O region of the right half of the tiled image, these interconnects connect to the foldable mesh I/O pads (Figure 1B, iii). In their planar, unfolded state, the I/O pads are about twice as large as the I.D. of the capillary tube used for injection (see Materials and Methods in Supporting Information for details of key mesh dimensions and parameters). Short nonconducting SU-8 elements connecting neighboring mesh I/O pads together are also visible, included in the design to maintain pad order and spacing after injection.

Initially, we evaluated loading of the plug-and-play mesh electronics design into capillary syringe needles (Materials and Methods in Supporting Information). First, plug-and-play meshes were released from their substrates and suspended in 1X phosphate buffered saline (PBS) solution within a clear beaker. Second, the free end of a 400 μm I.D. glass capillary needle, which was connected to a syringe, was positioned close to the I/O end of the mesh structure, and then the syringe was used to draw the entire mesh electronics probe into the capillary needle. A representative image of a mesh-loaded capillary needle (Figure 2A) highlights the key features of the mesh design, including the I/O pads at the top of the image, the narrow stem region in middle, and the ultraflexible mesh device region near the bottom of the tube. A magnified view of the I/O region inside the capillary tube (Figure 2B) shows the mesh I/O pads rolled-up within the confined volume of the tube.

To investigate the injection characteristics and I/O interfacing scheme of the plug-and-play mesh electronics, we first injected into 0.5% agarose hydrogel, which has mechanical properties similar to those of brain tissue and has been used previously as an in vitro model medium (Materials and Methods in Supporting Information).[15,29,30] Mesh electronics probes loaded in capillary needles were injected using our reported FoV method,[15] in which the capillary tube is retracted at the same rate with which the mesh is injected, enabling precise spatial targeting without crumpling of the ultraflexible mesh. The typical injection volumes were less than 50 μL per

DOI: 10.1021/acs.nanolett.7b03081
Nano Lett. 2017, 17, 5836−5842

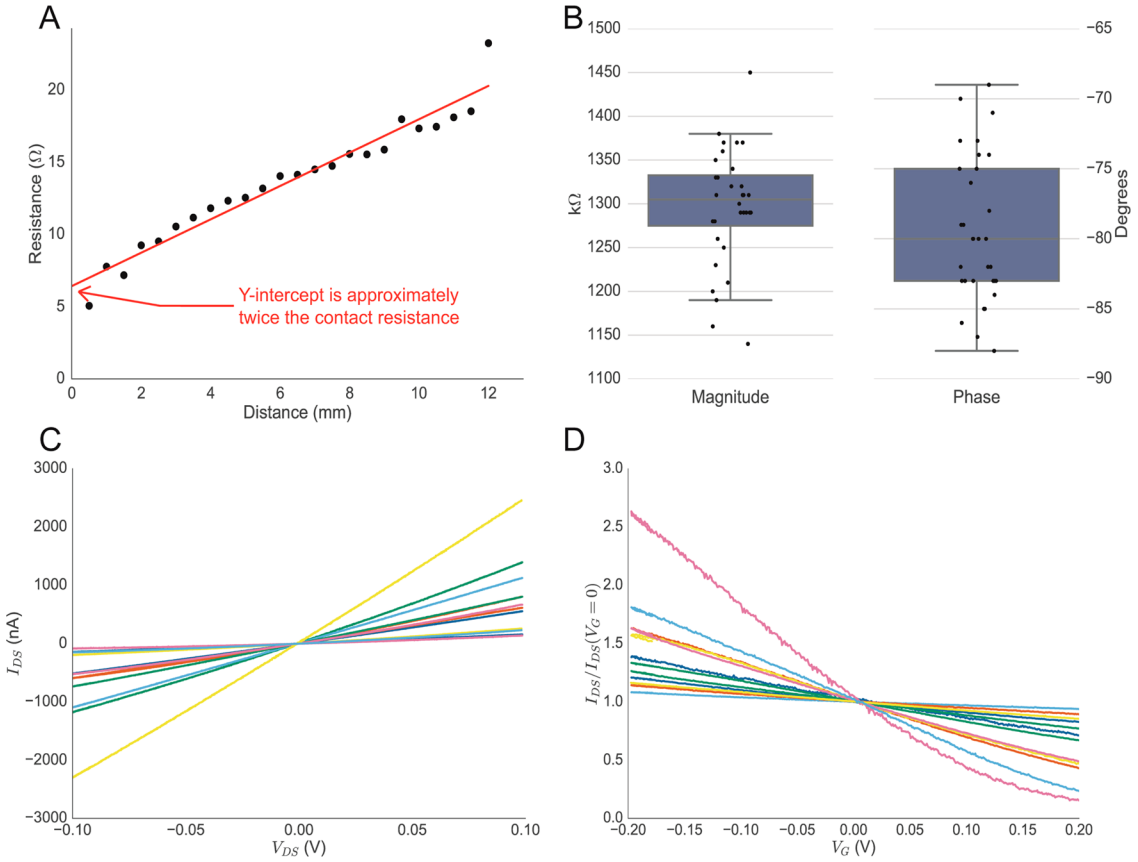

Figure 3. Electrical characterization of clamp-connected mesh electronics. (A) Four-point probe measurements of resistance versus distance for a ZIF-clamped mesh I/O pad. The *y*-intercept is approximately twice the contact resistance R_c, yielding $R_c \cong 3\ \Omega$. (B) Box plot of interfacial impedance magnitude and phase at 1 kHz for 32 independently addressable Pt electrodes in a ZIF-clamped mesh. All electrodes are 20 μm diameter and characterized while immersed in 1X PBS. The box lines correspond to the first, second, and third quartiles, and the whiskers extend to the last data point within 1.5-times the interquartile range of the nearest quartile. Data points for all 32 electrodes are plotted as black dots. (C) $I_{DS}-V$ curves for 12 NW-FETs in a ZIF-clamped mesh injected into 1X PBS. (D) Water gate responses for the 12 NW-FETs shown in panel C.

~4 mm length of mesh, which is comparable to volumes for the standard mesh electronics design.[15,17] The injection process was completed when the I/O region was ejected from the capillary tube onto a thin-film clamping substrate and the pads were rinsed with drops of water to remove remaining saline. Importantly, an image of the I/O region (Figure 2C) demonstrates that the mesh I/O pads unroll to their extended, planar configuration necessary for plug-and-play connection.

The loading and injection experiments highlight several points. First, plug-and-play mesh electronics can be injected with the same capillary tube diameter, flow rates, injection volumes, and FoV method used in previous syringe-injectable mesh electronics studies.[14,15,17,18] Since the mesh structure injected into the brain is unchanged from the standard mesh design, no compromises in the attractive tissue response and in vivo chronic recording are expected from the additional plug-and-play functionality. Second, I/O pads twice as large as the diameter of the injecting needle readily roll-up and subsequently unroll to a well-defined planar geometry during loading and ejection, respectively. Third, connecting the I/O pads through the thin film-like stem avoids potential tangling and random pad placement that can occur with previous all-mesh designs[15,17] and yields a deterministic linear spacing of I/O pads that is necessary for compatibility with a connector.

The connection of the mesh I/O pads was achieved in several straightforward steps (Materials and Methods in Supporting Information). First, to facilitate insertion into a ZIF connector mounted on a custom-designed printed circuit board (PCB, Figure S2), a tweezer was used to bend the stem region to a near 90° angle. The edge of the thin-film clamping substrate was trimmed with a scissor close to the outer edge of the I/O pads (arrow, Figure 2C). The I/O pads were then manually inserted into the ZIF connector (Figure 2D) and the latch engaged to electrically contact the I/O pads with the ZIF connector pins. Release of the ZIF latch following closure and subsequent inspection of the I/O pads (dashed box, Figure 2E) shows rectangular indentations where the ZIF connector pins made clear contact to the mesh I/O pads. Estimates of the mechanical contact yield made by counting the number of I/O pads with single pin indentations (i.e., 1:1 contact without shorting to adjacent channels) showed that we could reliably achieve yields of 100% to all I/O pads inserted to the appropriate depth within the ZIF connector. In cases in which the pads were not mechanically contacted on the first attempt, it was always possible to adjust the insertion depth of the I/O pads until 1:1 contact was achieved.

These connection results illustrate a few important features of the plug-and-play I/O design. First, alignment between the ZIF connector pins and the mesh I/O pads in the longitudinal direction (parallel to the mesh and capillary tube axes) can be nearly guaranteed by designing the I/O pad width and pitch to match the ZIF connector. For the ZIF connector used here, for

DOI: 10.1021/acs.nanolett.7b03081
Nano Lett. 2017, 17, 5836−5842

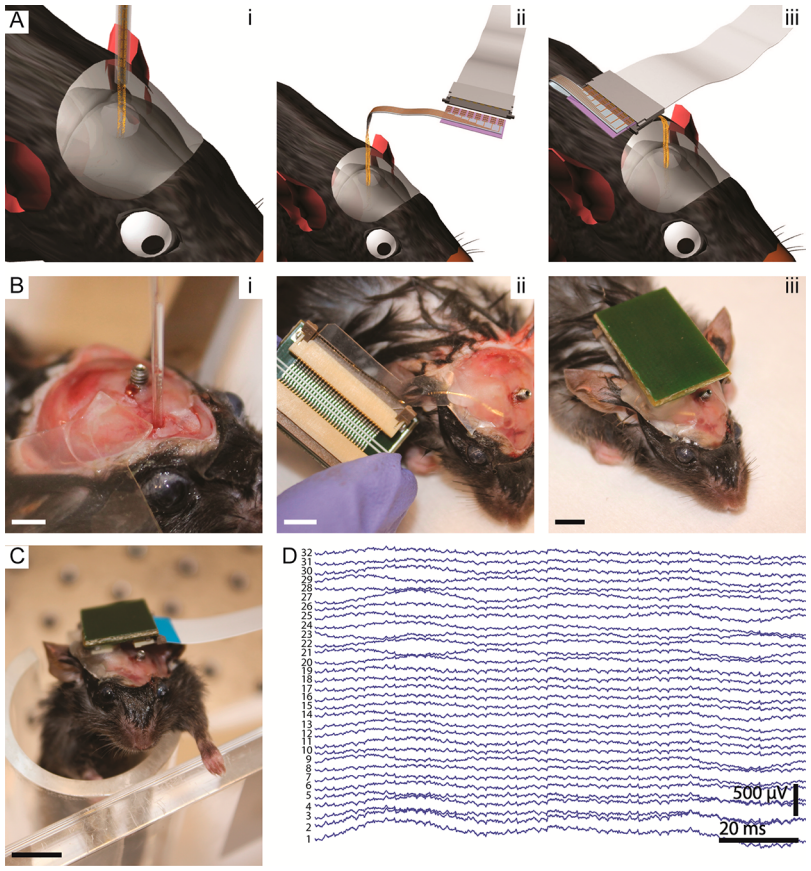

Figure 4. Plug-and-play mesh electronics for in vivo neural recording. (A) Schematic illustrating key steps of the clamp-connect I/O interfacing procedure as applied to in vivo mouse brain studies. (i) Mesh is stereotaxically injected into the brain region of interest using the FoV method. (ii) Mesh I/O pads are ejected onto a thin-film clamping substrate tape and then the tape is cut with scissors to the pad edges for insertion into a PCB-mounted ZIF connector. (iii) PCB is cemented into place on the mouse skull, forming a compact head-stage for acute and chronic studies. (B) Photographs (i–iii) show the same key steps in the schematics in (A) for the I/O interfacing procedure in the case of a male C57BL/6J mouse. Scale bars are 2 mm, 5 mm, and 5 mm, respectively. (C) Photograph of a male C57BL/6J mouse in a restrainer during a recording session. The FFC inserted into the PCB (upper right) connects to the recording instrumentation. Scale bar is 1 cm. (D) Representative traces for multiplexed in vivo LFP recording from 32 Pt electrodes. The channels are numbered 1–32 from deepest to shallowest location within the brain. Signals were sampled at 20 kHz with a 60 Hz notch filter applied at the time of acquisition and are otherwise unprocessed.

example, the pin width $a \cong 100$ μm and the pin pitch $p = 500$ μm. The optimum choice for the I/O pads is then also pitch $p = 500$ μm and pad width $b = p - a = 400$ μm (Figure S3).[31] With these selections, the mesh I/O pads can be inserted blindly into the ZIF connector with a nearly 100% chance of 1:1 electrical interfacing (i.e., no open or shorted channels). Second, alignment between the ZIF connector pins and the I/O pads in the transverse direction (normal to the mesh and capillary tube axes) is accomplished by using I/O pads made of a macroporous mesh structure, which allows the I/O pads to be at least twice as large as the capillary tube I.D. without adversely affecting the injection mechanics. The resulting I/O pads are at least about 1 mm long, which is long enough for manual, naked-eye alignment to the appropriate insertion depth within the ZIF connector. Together, these two design features make possible facile "by hand" plug-and-play connection to mesh electronics. Third, the entire post-injection positioning/clamping procedure usually takes only 5–10 min and is constant regardless of channel count. The mesh designs used here contained 32 channels, but the time required to interface to an even larger number of channels will be approximately the same as long as only a single ZIF connector is required.

We have carried out several characterization studies to validate the electrical performance of the plug-and-play clamp-connect interface as well as the mesh electronics devices connected through the new interface. To measure the contact resistance between the ZIF connector pins and the mesh I/O pads, we fabricated a large area mesh I/O pad and clamped it with a ZIF connector (Materials and Methods in Supporting Information) using the same electrical interfacing procedure described above for plug-and-play mesh electronics (Figure S4A). Four-point probe measurements of resistance versus distance measured from various ZIF connector channels produced data with a linear dependence ($r^2 = 0.94$; Figure 3A). The y-intercept represents the fixed component of the resistance, predominantly attributable to two series pad-to-pin contact resistances (Figure S4B), yielding a contact resistance $R_c \cong 3$ Ω. This contact resistance is 1–3 orders of magnitude smaller than previously reported bonding resistances of 4.2 kΩ and 33.7 Ω for conductive ink and ACF bonding, respectively.[14,15]

We electrically characterized the device performance for plug-and-play mesh electronics incorporating either Pt electrodes or Si NW-FETs (Materials and Methods in Supporting Information). The 1 kHz interfacial impedance determined

DOI: 10.1021/acs.nanolett.7b03081
Nano Lett. 2017, 17, 5836–5842

from measurements of 32 Pt electrodes in a ZIF-clamped mesh probe following injection into 1X PBS (Figure 3B) yielded a mean impedance magnitude and phase values of 1.3 MΩ and −80°, respectively, as expected for a nearly perfectly polarizable electrode.[32] This impedance is in line with values reported in the literature and is near the theoretical purely capacitive interfacial impedance for a 20 μm diameter Pt electrode of about 930 kΩ.[14,33−35] Frequency-dependent impedance measurements of mesh electronics were used to compare the electrode interfacial impedance to the impedance between adjacent interconnect channels in the stem region over a frequency range of 10 Hz to 10 kHz (Figure S5). These data show approximately three orders of magnitude greater impedance between adjacent stem interconnects compared to electrodes and the recording medium, implying minimal cross-talk between channels over physiologically relevant recording frequencies. This measurement represents the worst-case scenario since in actual in vivo measurements the stem interconnects are surrounded by lower dielectric constant air or dental cement instead of the 1X PBS used in the impedance measurement. In addition, the properties of a mesh electronics probe incorporating 12 Si NW-FET devices were characterized after injection into 1X PBS and connection by the plug-and-play interface. Current versus drain-source voltage ($I-V_{DS}$) sweeps (Figure 3C) yielded linear output characteristics for all 12 devices, indicating ohmic contacts to the NW-FETs and the mesh electronics probe over the sweep range of ±100 mV. Transfer characteristics measured with V_{DS} = 100 mV and water gate voltage (V_G) swept over ±200 mV showed a clear p-type gate response for all 12 NW-FETs (Figure 3D). Together, these results highlight the excellent performance and generality of the plug-and-play I/O strategy. The small contact resistance of 3 Ω minimizes series resistance, which would otherwise contribute to power loss and reduce effective transconductance in FETs,[36] and thus makes the approach suitable for low noise and low power electronics and ultrasensitive conductance-based sensing devices.[19]

Last, we have explored and validated the plug-and-play mesh electronics for in vivo mouse brain recording. A schematic of our approach exemplified with a rodent model (Figure 4A) highlights several key points. First, we stereotaxically inject mesh electronics with the FoV method using the same method successfully validated in previous work (Figure 4A, i).[15,17] Second, the I/O pads are ejected onto a thin-film clamping substrate tape, and the stem is bent smoothly to a near 90° angle above the first I/O pad. The substrate tape is cut with scissors to the pad edges, and then the pads are inserted into the PCB-mounted ZIF connector (Figure 4A, ii). Last, we fold the PCB onto the back of the mouse's skull and fix it in place with dental cement (Figure 4A, iii).[17] The PCB serves as a compact head-stage for recording studies by inserting a FFC, which is connected to recording instrumentation, at the time of the measurements.

We validated the procedure by stereotaxic injection of a plug-and-play mesh containing 32 Pt electrodes into a mouse brain (Materials and Methods in Supporting Information). Photographs of key steps in the procedure similar to the schematics (Figure 4B) highlight critical points. First, the mesh was injected into the right cerebral hemisphere using the FoV method with a total injected saline volume less than 50 μL (Figure 4B, i). Given the injection coordinates and mesh electronics design, which spreads the 32 electrodes over a depth of 2 mm, the recording electrodes are implanted approximately in the caudoputamen region of the brain. Second, after ejection of the mesh I/O pads onto the substrate tape, the stem was manually bent with a tweezer to allow room for insertion into the ZIF connector, and then the substrate tape was trimmed to the edge of the I/O pads. This I/O portion was then inserted into the ZIF connector and the connector latched (Figure 4B, ii). Last, the PCB was turned over and sealed to the skull within the surgery region, taking care to maintain access to the grounding screw and the second ZIF connector (Figure 4B, iii). The resulting PCB head-stage weighed only 1.54 g and was easily interfaced to peripheral amplifier and recording electronics by inserting a FFC (Figure 4C). An acute recording session approximately 1 h after injection yielded the expected LFP signals from 32/32 electrode channels (Figure 4D).[14,17]

In conclusion, we have described a new plug-and-play syringe-injectable mesh electronics design and accompanying clamp-connect I/O interfacing scheme that is rapid, scalable, and user-friendly to nonexperts. It combines the advantages of an ultraflexible device region that seamlessly integrates with brain tissue in vivo with the convenience of an I/O region that can be facilely interfaced "by hand" in minutes via a PCB-mounted ZIF connector. Injections into brain-mimicking hydrogel demonstrated delivery of plug-and-play mesh electronics through capillary needles with precise targeting using microliter-scale injection volumes. Electrical characterization of mesh electronics containing Pt electrodes and NW-FETs showed the plug-and-play design and ZIF connection scheme can be used to interface to arbitrary devices with a contact resistance of only 3 Ω. Last, a plug-and-play mesh electronics probe was validated for in vivo mouse studies where syringe-injection was used for implantation of the mesh probe, only minutes were required for I/O connection, and subsequent measurements yielded LFP recordings from 100% of the 32 channels.

Significantly, the plug-and-play interfacing procedure requires only common, commercially available supplies, which are simple to sterilize for a surgical environment and result in a compact PCB head-stage compatible with both acute and chronic recording experiments. The PCB head-stage could serve as a convenient platform for implementing additional electronic functionality in future experiments such as digital multiplexing,[35,37] wireless communications,[37−39] and signal processing.[37] Our results expand substantially the potential applications of syringe-injectable mesh electronics, significantly lower barriers to use by new investigators, and pave the way for increasingly sophisticated mesh electronics designs for use in both basic neuroscience and clinical studies.

■ ASSOCIATED CONTENT

Supporting Information

The Supporting Information is available free of charge on the ACS Publications website at DOI: 10.1021/acs.nanolett.7b03081.

Materials and methods; design of plug-and-play mesh electronics with NW-FETs; custom PCB for clamp-connection to mesh electronics; optimum geometry for I/O pad design; four-point probe measurements of contact resistance; frequency-dependent impedance of plug-and-play mesh electronics channels; supplementary references (PDF)

DOI: 10.1021/acs.nanolett.7b03081
Nano Lett. 2017, 17, 5836−5842

AUTHOR INFORMATION

Corresponding Author

*E-mail: cml@cmliris.harvard.edu.

ORCID

Charles M. Lieber: 0000-0002-6660-2456

Author Contributions

T.G.S. and J.Y. contributed equally to this work.

Notes

The authors declare no competing financial interest.

ACKNOWLEDGMENTS

C.M.L. acknowledges support of this work by the Air Force Office of Scientific Research (FA9550-14-1-0136). T.G.S. acknowledges support by the Department of Defense (DoD) through the National Defense Science & Engineering Graduate Fellowship (NDSEG) program. G.H. acknowledges fellowship support from the American Heart Association (16POST27250219). This work was performed in part at the Harvard University Center for Nanoscale Systems (CNS), a member of the National Nanotechnology Coordinated Infrastructure Network (NNCI), which is supported by the National Science Foundation under NSF ECCS Award No. 1541959.

REFERENCES

(1) Cash, S. S.; Hochberg, L. R. *Neuron* **2015**, *86*, 79−91.
(2) Lutcke, H.; Margolis, D. J.; Helmchen, F. *Trends Neurosci.* **2013**, *36*, 375−384.
(3) Yuste, R. *Nat. Rev. Neurosci.* **2015**, *16*, 487−497.
(4) Buzsaki, G. *Neuron* **2010**, *68*, 362−385.
(5) Carandini, M. *Nat. Neurosci.* **2012**, *15*, 507−509.
(6) Hochberg, L. R.; Bacher, D.; Jarosiewicz, B.; Masse, N. Y.; Simeral, J. D.; Vogel, J.; Haddadin, S.; Liu, J.; Cash, S. S.; van der Smagt, P.; Donoghue, J. P. *Nature* **2012**, *485*, 372−375.
(7) Shenoy, K. V.; Carmena, J. M. *Neuron* **2014**, *84*, 665−680.
(8) Truccolo, W.; Ahmed, O. J.; Harrison, M. T.; Eskandar, E. N.; Cosgrove, G. R.; Madsen, J. R.; Blum, A. S.; Potter, N. S.; Hochberg, L. R.; Cash, S. *J. Neurosci.* **2014**, *34*, 9927−9944.
(9) Cook, M. J.; O'Brien, T. J.; Berkovic, S. F.; Murphy, M.; Morokoff, A.; Fabinyi, G.; D'Souza, W.; Yerra, R.; Archer, J.; Litewka, L.; Hosking, S.; Lightfoot, P.; Ruedebusch, V.; Sheffield, W. D.; Snyder, D.; Leyde, K.; Himes, D. *Lancet Neurol.* **2013**, *12*, 563−571.
(10) Seymour, J. P.; Wu, F.; Wise, K. D.; Yoon, E. *Microsystems & Nanoengineering* **2017**, *3*, 16066.
(11) Bensmaia, S. J.; Miller, L. E. *Nat. Rev. Neurosci.* **2014**, *15*, 313−325.
(12) Perge, J. A.; Homer, M. L.; Malik, W. Q.; Cash, S.; Eskandar, E.; Friehs, G.; Donoghue, J. P.; Hochberg, L. R. *J. Neural Eng.* **2013**, *10*, 036004.
(13) Scholvin, J.; Kinney, J. P.; Bernstein, J. G.; Moore-Kochlacs, C.; Kopell, N.; Fonstad, C. G.; Boyden, E. S. *IEEE Trans. Biomed. Eng.* **2016**, *63*, 120−130.
(14) Liu, J.; Fu, T. M.; Cheng, Z.; Hong, G.; Zhou, T.; Jin, L.; Duvvuri, M.; Jiang, Z.; Kruskal, P.; Xie, C.; Suo, Z.; Fang, Y.; Lieber, C. M. *Nat. Nanotechnol.* **2015**, *10*, 629−636.
(15) Hong, G.; Fu, T. M.; Zhou, T.; Schuhmann, T. G.; Huang, J.; Lieber, C. M. *Nano Lett.* **2015**, *15*, 6979−6984.
(16) Xie, C.; Liu, J.; Fu, T. M.; Dai, X.; Zhou, W.; Lieber, C. M. *Nat. Mater.* **2015**, *14*, 1286−1292.
(17) Fu, T. M.; Hong, G.; Zhou, T.; Schuhmann, T. G.; Viveros, R. D.; Lieber, C. M. *Nat. Methods* **2016**, *13*, 875−882.
(18) Zhou, T.; Hong, G.; Fu, T. M.; Yang, X.; Schuhmann, T. G.; Viveros, R. D.; Lieber, C. M. *Proc. Natl. Acad. Sci. U. S. A.* **2017**, *114*, 5894−5899.
(19) Zhang, A.; Lieber, C. M. *Chem. Rev.* **2016**, *116*, 215−257.
(20) Budday, S.; Nay, R.; de Rooij, R.; Steinmann, P.; Wyrobek, T.; Ovaert, T. C.; Kuhl, E. *J. Mech. Behav. Biomed. Mater.* **2015**, *46*, 318−330.
(21) Polikov, V. S.; Tresco, P. A.; Reichert, W. M. *J. Neurosci. Methods* **2005**, *148*, 1−18.
(22) Grill, W. M.; Norman, S. E.; Bellamkonda, R. V. *Annu. Rev. Biomed. Eng.* **2009**, *11*, 1−24.
(23) Luan, L.; Wei, X.; Zhao, Z.; Siegel, J. J.; Potnis, O.; Tuppen, C. A.; Lin, S.; Kazmi, S.; Fowler, R. A.; Holloway, S.; Dunn, A. K.; Chitwood, R. A.; Xie, C. *Sci. Adv.* **2017**, *3*, e1601966.
(24) Liu, J.; Xie, C.; Dai, X.; Jin, L.; Zhou, W.; Lieber, C. M. *Proc. Natl. Acad. Sci. U. S. A.* **2013**, *110*, 6694−6699.
(25) Tian, B.; Liu, J.; Dvir, T.; Jin, L.; Tsui, J. H.; Qing, Q.; Suo, Z.; Langer, R.; Kohane, D. S.; Lieber, C. M. *Nat. Mater.* **2012**, *11*, 986−994.
(26) Yao, J.; Yan, H.; Lieber, C. M. *Nat. Nanotechnol.* **2013**, *8*, 329−335.
(27) Reina, A.; Jia, X.; Ho, J.; Nezich, D.; Son, H.; Bulovic, V.; Dresselhaus, M. S.; Kong, J. *Nano Lett.* **2009**, *9*, 30−35.
(28) Jiao, L.; Fan, B.; Xian, X.; Wu, Z.; Zhang, J.; Liu, Z. *J. Am. Chem. Soc.* **2008**, *130*, 12612−12613.
(29) Chen, Z.-J.; Gillies, G. T.; Broaddus, W. C.; Prabhu, S. S.; Fillmore, H.; Mitchell, R. M.; Corwin, F. D.; Fatouros, P. P. *J. Neurosurg.* **2004**, *101*, 314−322.
(30) Deepthi, R.; Bhargavi, R.; Jagadeesh, K.; Vijaya, M. S. *SAS Tech J.* **2010**, *9*, 27−30.
(31) Gillett, J. B.; Washo, B. D. Connector and Cable Packaging. In *Microelectronics Packaging Handbook*; Tummala, R. R., Rymaszewski, E. J., Eds.; Von Nostrand Reinhold: New York, 1989; pp 955−1020.
(32) Cogan, S. F. *Annu. Rev. Biomed. Eng.* **2008**, *10*, 275−309.
(33) Franks, W.; Schenker, I.; Schmutz, P.; Hierlemann, A. *IEEE Trans. Biomed. Eng.* **2005**, *52*, 1295−1302.
(34) Cheung, K. C.; Renaud, P.; Tanila, H.; Djupsund, K. *Biosens. Bioelectron.* **2007**, *22*, 1783−1790.
(35) Berenyi, A.; Somogyvari, Z.; Nagy, A. J.; Roux, L.; Long, J. D.; Fujisawa, S.; Stark, E.; Leonardo, A.; Harris, T. D.; Buzsaki, G. *J. Neurophysiol.* **2014**, *111*, 1132−1149.
(36) Sze, S. M. *Physics of Semiconductor Devices*; John Wiley & Sons, 1981.
(37) Sodagar, A. M.; Perlin, G. E.; Yao, Y.; Najafi, K.; Wise, K. D. *IEEE J. Solid-State Circuits* **2009**, *44*, 2591−2604.
(38) Wentz, C. T.; Bernstein, J. G.; Monahan, P.; Guerra, A.; Rodriguez, A.; Boyden, E. S. *J. Neural Eng.* **2011**, *8*, 046021.
(39) Harrison, R. R.; Kier, R. J.; Chestek, C. A.; Gilja, V.; Nuyujukian, P.; Ryu, S.; Greger, B.; Solzbacher, F.; Shenoy, K. V. *IEEE Trans. Neural Syst. Rehabil. Eng.* **2009**, *17*, 322−329.

DOI: 10.1021/acs.nanolett.7b03081
Nano Lett. 2017, 17, 5836−5842